Topological phases in the TaSe_{3} compound

Simin Nie, Lingyi Xing, Rongying Jin, Weiwei Xie, Zhijun Wang, and Fritz B. Prinz

Phys. Rev. B **98**, 125143 — Published 26 September 2018

DOI: 10.1103/PhysRevB.98.125143

Topological phases in the $TaSe_3$ compound

Simin Nie[1], Lingyi Xing[2], Rongying Jin[2], Weiwei Xie[3], Zhijun Wang[4],[*] and Fritz B. Prinz[1]
[1] *Department of Materials Science and Engineering,*
Stanford University, Stanford, California 94305, USA
[2] *Department of Physics and Astronomy, Louisiana State University, Baton Rouge, LA, 70803, USA*
[3] *Department of Chemistry, Louisiana State University, Baton Rouge, LA, 70803, USA and*
[4] *Department of Physics, Princeton University, Princeton, New Jersey 08544, USA*
(Dated: September 10, 2018)

Based on first-principles calculations, we show that stoichiometric $TaSe_3$, synthesized in space group $P2_1/m$, belongs to a three-dimensional (3D) strong topological insulator (TI) phase with Z_2 invariants (1;100). The calculated surface spectrum shows clearly a single Dirac cone on surfaces, with helical spin texture at a constant energy contour. To check the stability of the topological phase, strain effects have been systematically investigated, showing that many topological phases survive in a wide range of the strains along both the a- and c-axes, such as strong TI (STI), weak TI (WTI) and Dirac semimetal phases. $TaSe_3$ provides us an ideal platform for experimental study of topological phase transitions. More interestingly, since superconductivity in $TaSe_3$ has been reported for a long time, the co-existence of topological phases and superconducting phase suggests that $TaSe_3$ is a realistic system to study the interplay between topological and superconducting phases in the future.

I. INTRODUCTION

The layered transition-metal trichalcogenides MX_3 (M=Nb, Ta; X=S, Se) have attracted lots of interest because of the appearance of the charge-density-wave (CDW) states at low temperature (LT)[1–4]. For instance, both TaS_3[3] and $NbSe_3$[5] are metals at room temperature (RT), and undergo two different CDW transitions as decreasing temperature. But $TaSe_3$ is an exception, in which no CDW transition has been found yet[6]. Instead, $TaSe_3$ remains semimetallic from RT to LT and becomes superconducting at T_c = 2.3 K[7–9]. The earlier theoretical studies[10] suggest that it could be either a semiconductor or a semimetal, depending on the relative energy level of an anti-bonding Se p band to that of the Ta d_{z^2} band. So far, first-principles calculations of $TaSe_3$ have not been reported yet, and the electronic structures, Fermi surfaces and topological properties are still unrevealed.

Meanwhile, topological superconductors have attracted much interest due to the emergence of Majorana fermions[11,12] and the potential application in quantum computation[13]. The previous work by Fu *et al.*[14] has proposed that the topological superconductivity can be realized on the interface between a TI and a BCS superconductor by proximity effect[15–19]. Very recently, topological superconductivity has been observed on the surface of iron-based superconductors below T_c[20], which suggests that a more promising approach to engineer TSCs is to propose superconducting materials with non-trivial topology in their electronic structures[16]. Herein, this approach would avoid the structural compatibility and overcome the fabrication challenges related to the interfaces or heterostructures[16–19,21–23]. However, most superconductors do not have non-trivial bulk topology in electronic structures[15,24], and some topological candidates do need doping to induce superconductivity, like $Cu_xBi_2Se_3$[25,26], $FeTe_xSe_{1-x}$[16,20], *etc.* Therefore, it is challenging to find a superconductor with non-trivial electronic topology.

In this work, based on first-principles calculations, we show that the single crystal $TaSe_3$, known as a superconductor for many years[7–9], has non-trivial electronic structure. The crucial band inversion happens at B point even without spin-orbit coupling (SOC). This is different from the situation in Bi_2Se_3[27,28], in which the band inversion is due to the strong SOC effect. Our detailed analysis indicates that the band inversion is attributed to the "broken" type II chains, especially the Se3-Ta1 and Se6-Ta2 bonds. To shorten these bonds by compressive strains would enlarge the band gap and remove the band inversion. Inclusion of SOC in $TaSe_3$ opens a continuous direct gap in the entire Brillouin zone (BZ), but doesn't change the energy ordering of the bands at the time-reversal invariant momentum (TRIM) points. The Z_2 invariants (ν_0;ν_1,ν_2,ν_3)[29,30] are calculated to be (1;100). The strong topological index $\nu_0 = 1$ guarantees the existence of the Dirac-cone states on surfaces[31], which has been further confirmed by our surface calculations. To check the stability of the topological phase, strain effects have been systematically investigated, showing that many topological phases survive in a wide range of the strains along both the a- and c-axes, such as STI, WTI and Dirac semimetal phases. It's an ideal platform for experimental study of topological phase transitions. As it becomes superconducting below T_c, $TaSe_3$ also provides us a realistic system to investigate the interplay between the topological surface states and superconductivity.

This paper is organized as follows. In Sec. II we will introduce the details of first-principles calculations. In Sec. III, the calculation results are presented. Finally, Sec. IV contains the discussion and conclusion.

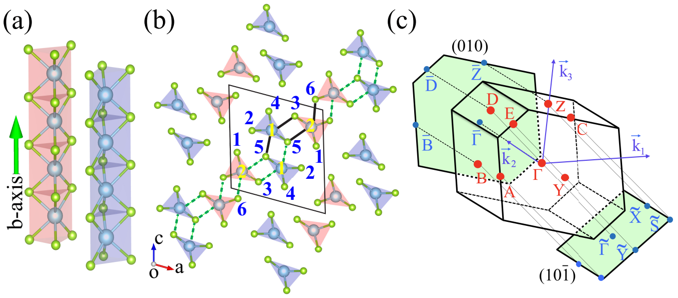

FIG. 1. (Color online) Crystal structure and BZs of $TaSe_3$. (a) The side view of the type I and type II chains colored in blue and red, respectively. Two neighbor prisms are differed by $b/2$ in the b-direction, making the Ta atoms in the planes of the Se_3 triangles of the neighbor prism. (b) The projection view along the chain direction (*i.e.*, the b-direction). The primitive unit cell is shown in light black parallelogram. The nonequivalent Ta atoms (large balls) and Se atoms (small balls) in the primitive unit cell are labeled by yellow and light blue numbers, respectively. The bonds (green dashed lines) of Se5-Ta1-Se3 and Se5-Ta2-Se6 make the prisms form a layer (spanned by the b-axis and $(a+c)$-axis). (c) Bulk BZ, projected surface BZs, and high-symmetry points.

II. CALCULATION METHOD

The first-principles calculations were performed within the framework of full-potential linearized-augmented plane-wave (FP-LAPW) method implemented in WIEN2K simulation package[32]. Modified Becke-Johnson exchange potential together with local density approximation for the correlation potential was used to obtain accurate band structures[33]. SOC was included as a second variational step self-consistently. The radii of the muffin-tin sphere (RMT) were 2.5 Bohr for Ta and 2.38 Bohr for Se, respectively. The k-points sampling grid of the BZ in the self-consistent process was $7 \times 19 \times 6$. The truncation of the modulus of the reciprocal lattice vector K_{max}, which was used for the expansion of the wave functions in the interstitial region, was set to $R_{MT} \times K_{max} = 7$. The geometry optimization including SOC interaction was carried out within the framework of the projector augmented wave (PAW) pseudopotential method implemented in Vienna *ab initio* simulation package (VASP)[34,35]. The ionic positions were relaxed until force on each ion was less than 0.005 eV $\AA^{-1}$. PHONOPY was employed to calculate the phonon dispersion through the DFPT method[36].

III. RESULTS

$TaSe_3$ crystallizes in the monoclinic layered structure with space group $P2_1/m$. The basic building blocks of $TaSe_3$ are parallel trigonal-prismatic chains along the b-axis, as shown in Fig. 1(a). Each chain is made by a linear stacking of irregular prismatic cages, which consists of six selenium atoms at the corners and one tantalum atom at the center. In the top view of Fig. 1(b), these chains are classified as type I (*i.e.*, $d_s^I = d_{24}$=2.57Å) and type II (*i.e.*, $d_s^{II} = d_{16}$=2.9Å), depending on the shortest bond (d_s) of an irregular triangle which is formed by three Se atoms. $TaSe_3$ has two type I and two type II chains in a unit cell. The two chains of each type are related by inversion symmetry. The four prismatic chains have strong bonds (*i.e.*, Se5-Ta1-Se3 and Se5-Ta2-Se6) along the $a+c$ direction, forming the $TaSe_3$ layers as depicted by green dashed lines. The interlayer hoppings are relatively weak compared with the intralayer hoppings, suggesting 2D $TaSe_3$ can be easily produced by exfoliation methods.

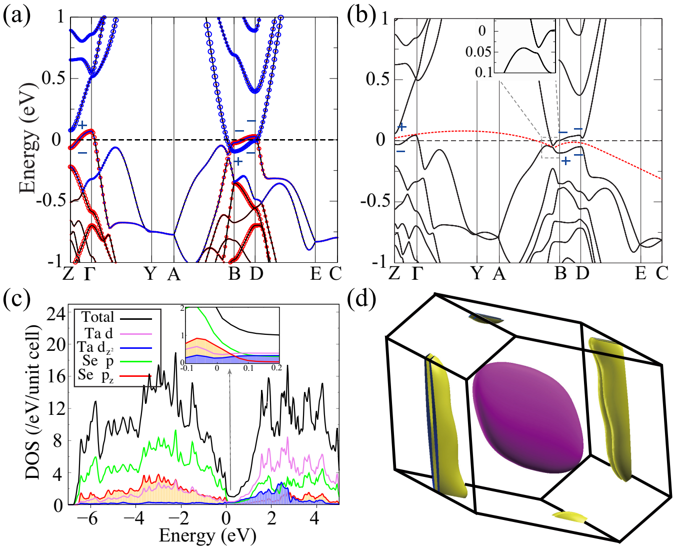

FIG. 2. (Color online) Electronic structures of $TaSe_3$ without (a) and with (b) SOC. The calculated parity eigenvalues of highest valence band (HVB) and the lowest conduct band (LCB) at B and D points are given explicitly. The size of red and blue circles in (a) represents the weights of Se3 p_z and Ta1 d_{z^2}, respectively. The inset in (b) shows the zoom-in band structure around the band crossing point located on the A-B line. The red dashed line in (b) indicates the existence of the continuous direct gap. (c) The calculated total DOS and PDOS of $TaSe_3$. The inset in (c) shows the DOS around the E_F. (d) The Fermi surface of $TaSe_3$.

Next, we discuss the qualitative electronic structure of $TaSe_3$ by way of a simple Zintl-Klemm concept[37]. In the type I chain of $TaSe_3$, where the distance between two Se atoms is short enough (*i.e.*, d_s^I=2.575 Å), a strong covalent p-p bond is formed. Thus, the oxidation state of the Se_3 triangle is ($Se^{2-} + Se_2^{2-}$). That's why $ZrSe_3$ is a semiconductor with Zr^{4+} and only type I chains[38]. However, in the type II chain, the distance is not short enough; namely, the p-p bond is broken. These Se atoms exhibit the normal oxidation states ($3Se^{2-}$). At the ionic limit, the chemical valence of tantalum is about 5+ (Ta^{5+}). Thus, $(TaSe_3)_4$ can be formulated as $2(4Se^{2-}+Se_2^{2-}+2Ta^{5+})$ in a primitive unit cell. According to this electron counting model, $TaSe_3$ would be a

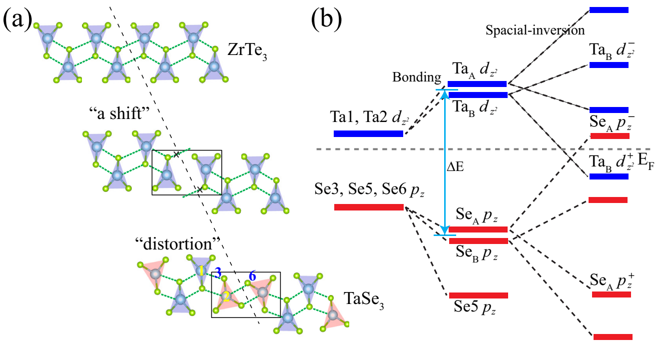

FIG. 3. (Color online) The evolution of the crystal structures and the schemetic diagram of the band-inversion mechanism. (a) The upper pattern is a layer of the ZrSe$_3$ structure, which is a semiconductor and only contains type I chain with Zr^{4+}, Se^{2-} and (Se)$_2^{2-}$ states. The middle pattern is the intermediate structure generated by a shift in the a-direction (the black dashed line), which breaks the previous bonds of Se3 atoms, denoted by the symbol "x". The lower pattern is a layer of the TaSe$_3$ structure. The distortion happens in the chains in the box, changing the type I chains to the type II chains. The new bonds between Se6 and Ta2 are built. (b) Schematic diagram of the band evolution in TaSe$_3$, starting from the atomic orbitals d_{z^2} of Ta1 and Ta2, and p_z of Se3, Se5 and Se6.

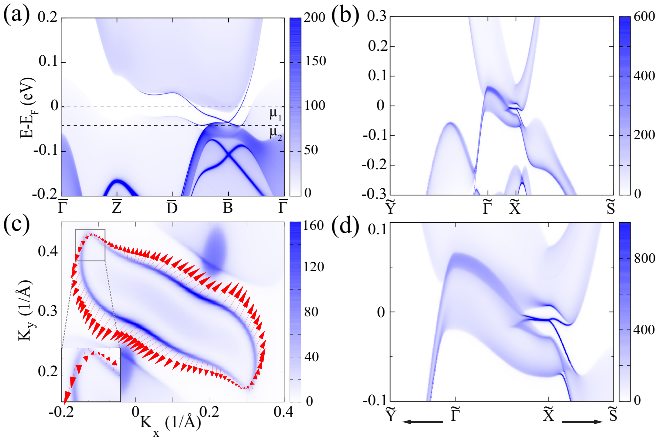

FIG. 4. (Color online) Surface states of TaSe$_3$. (a) and (b) are the surface band structures of TaSe$_3$ on the (010) and (10$\bar{1}$) surfaces, respectively. The chemical potentials at Fermi level (E$_F$) and 40 meV below the Fermi level are represented by μ_1 and μ_2, respectively. (c) The constant energy contour (E=E$_F$) of the topological surface states and corresponding spin texture on the (010) surface of TaSe$_3$. The inset shows the zoom-in Fermi surface around the upper left corner. (d) Zoom-in surface band structures around the Dirac point on the (10$\bar{1}$) plane.

semiconductor. However, TaSe$_3$ is metallic according to the transport measurements[39,40], which implies band inversion may occur in the electronic band structure. In order to fully understand the semimetallic propertes of TaSe$_3$, the first-principles calculations have been performed systematically.

When SOC is ignored, the calculated band structure along high symmetric lines in the BZ is shown in Fig. 2(a). There is always a direct gap between the conduction bands and valence bands, except two crossing points on the AB and DE lines. To elucidate the mechanism of the band inversion, we have calculated the projected weights on six nonequivalent Se atoms ($i.e.$, Se1, Se2, $\cdots$, and Se6, as shown in Fig. 1(b)) and two nonequivalent Ta atoms ($i.e.$, Ta1 and Ta2, as shown in Fig. 1(b)), respectively. In the fatted-band plot of Fig. 2(a), we denote the weights of Se3 p_z orbital ($\hat{z}||\vec{b}$) and Ta1 d_{z^2} orbital by the size of the red and blue circles, respectively. We can clearly see that the p_z band and the d_{z^2} band have an overlap at the Fermi level (E$_\mathrm{F}$). Further calculated results indicate that the up-going d_{z^2} band mainly comes from the d_{z^2} states of both Ta1 and Ta2, consistent with the ligand crystal splitting of five d orbitals in a prismatic cage. However, the down-going p_z band is mostly from the p_z orbitals of Se3 and Se6 atoms (both of them belong to the "broken" type II chains). To some extent, it suggests that the metallic band structure has to do with the type II chains. These similar results are also obtained by our calculated partial density of states (PDOS) in Fig. 2(c), which show that the Se p states and Ta d states are mainly located below and above the E$_\mathrm{F}$, respectively, with the hybridization between them. Near E$_\mathrm{F}$, the states are dominated by p_z states of Se3 and Se6 atoms and d_{z^2} states of Ta1 and Ta2 atoms.

To fully understand the metallic electronic band structure, we first investigate the crystal structure evolution beginning with the layered structure of ZrSe$_3$. In ZrSe$_3$ type I chains are arranged, as shown in Fig. 3(a), as a perfectly layered structure. It can be changed to the crystal structure of TaSe$_3$ by the following two steps. First, a shift may occur along the a-direction for every four prismatic chains (MX$_3$)$_4$, as shown in Fig. 3(a). As such, the bonds between selenium and tantalum atoms crossing the black dashed line are broken, as depicted by the symbol "x" in Fig. 3(a). Second, the distortion can happen in the prisms of the box by breaking the shortest p-p bonds between Se atoms. In addition, the new bonds between Ta2 and Se6 are built. Together, one can find that the crystal environment of Se3 and Se6 atoms of type II chains can change dramatically.

The band inversion can be understood from the bonds (green dashed lines) of Se5-Ta1-Se3 and Se5-Ta2-Se6, which support the layered structure of TaSe$_3$ (see Fig. 1(b) and Fig. 3(a)). In the atomic limit, the energy levels of the Ta d orbitals are higher than Se p orbitals. Under the crystal field of the prismatic cage, the d_{z^2} orbitals are lower than other d orbitals. The p_z orbitals of Se atom are higher than other p orbitals, since it doesn't orient toward the Ta atoms. Therefore, only p_z orbitals of Se3, Se5 and Se6, and d_{z^2} orbitals of Ta1 and Ta2 are considered in the schematic diagram of the band inversion, as shown in Fig. 3(b). Starting from the atomic limit, the energy level of the Ta d_{z^2} orbitals is higher

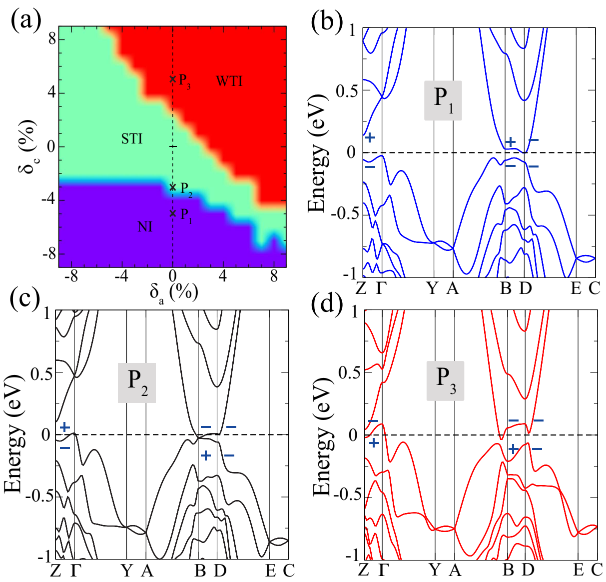

FIG. 5. (Color online) Phase diagram of $TaSe_3$ with strain along both a- and c-directions. (a) The blue, green and red regions represent NI, STI and WTI phases, respectively. (b), (c) and (d) are band structures of $TaSe_3$ with SOC for $c = 0.95c_0$ (P_1), $c = 0.97c_0$ (P_2) and $c = 1.05c_0$ (P_3), respectively. The parities of HVB and LCB at three TRIMs (B, D and Z) are given.

than that of the Se p_z orbitals. In step I, because Se5 forms two bonds while Se3 (or Se6) forms only one bond, the p_z state of Se5 is pushed much lower than the p_z state of Se3 (or Se6). The hybridization makes the two p_z orbitals of Se3 and Se6 form two mixed states, called Se_A and Se_B, respectively. Similarly, the two mixed states of Ta d_{z^2} orbitals are called Ta_A and Ta_B. The energy levels are illustrated in the middle of Fig. 3(b). In step II, the inversion symmetry is taken into consideration. Each state can split into two hybridized states, one bonding state and one antibonding state, according to the parity. The band inversion in $TaSe_3$ happens between the bonding state of Ta_B and antibonding state of Se_A, which is consistent with our fatted band calculations and PDOS. This band inversion mechanism is further confirmed by the phase diagram under strains, as will be shown later.

The inclusion of SOC leads to gap opening at the band crossing points, as seen in the band structure of Fig. 2(b). However, the maximum of the valence bands is still higher than the minimum of the conduction bands, which gives rise to the semimetallic properties of $TaSe_3$. The calculated Fermi surfaces consist of a large hole pocket enclosing Γ point and two electron pockets near B point, as shown in Fig. 2(d). Further parity analysis indicates that the inverted two bands have different parity eigenvalues at B point, while they have the same eigenvalue (*i.e.*, -1) at D point. Note that the band inversion has already happened even without SOC. The band inversion is attributed to the unique structure of the type II chains, especially the Se3-Ta1 and Se6-Ta2 bonds, which is distinct from the SOC-induced band inversion of the well-known Bi_2Se_3 family.

To classify TIs, one needs to compute four Z_2 topological indices $(\nu_0; \nu_1, \nu_2, \nu_3)$, where ν_0 is a strong topological index and (ν_1, ν_2, ν_3) are three weak topological indices. Since there is a continuous direct SOC gap, the Fu-Kane Z_2 invariants are well defined for the occupied bands below the gap in $TaSe_3$. Due to the existence of inversion center in $TaSe_3$, they can be easily calculated by Fu-Kane parity criterion[31] at eight TRIM points $(\Gamma_i, i = 1, 2, \ldots 8)$. The strong topological index is given by $(-1)^{\nu_0} = \prod_{i=1}^{8} \delta(\Gamma_i)$, where $\delta(\Gamma_i)$ is the product of parity eigenvalues of the bands at Γ_i without counting their time reversal partners. Three weak topological indices are defined at the four TRIM points in a plane offset from Γ point. Explicitly, $(-1)^{\nu_1} = \delta(A)\delta(B)\delta(D)\delta(E)$, $(-1)^{\nu_2} = \delta(A)\delta(C)\delta(E)\delta(Y)$ and $(-1)^{\nu_3} = \delta(C)\delta(D)\delta(E)\delta(Z)$. The space group of $TaSe_3$ is non-symmorphic with a screw symmetry $\bar{C}_{2b}$, which is a twofold rotation about the $\vec{b}$-axis followed by a half lattice translation in the same direction $(\vec{b}/2)$. It satisfies the relation $\bar{C}_{2b} I = t(\vec{b}) I \bar{C}_{2y}$, where I is inversion symmetry and the lattice translation $t(\vec{b})$ can be represented by a phase factor in the Bloch basis: $t(\vec{b}) = exp(-i\vec{b} \cdot \vec{k})$. Thus, at the TRIM points in the $\vec{k}_2 = \pi/b$ plane, *i.e.*, A, C, E and Y, with the expression $t(\vec{b}) = -1$, $\bar{C}_{2b}$ anticommutates with I. In combination of time reversal symmetry, the anticommutating relation leads that all the states are four-fold degenerate, consisting of two parity $+1$ bands and two parity -1 bands (*i.e.*, "$++--$"). Considering that the total number of valence bands is $68 = 4 \times 17$, we get $\delta(A) = \delta(C) = \delta(E) = \delta(Y) = (-1)^{17} = -1$. Therefore, the strong topological index ν_0 is determined by band inversion at other four TRIMs (Z, Γ, B and D). Their parity products are calculated to be $\delta(Z) = \delta(\Gamma) = \delta(D) = -1$ and $\delta(B) = 1$, which are extracted from standard numerical calculations based on first-principles calculations. Therefore, the Z_2 topological invariants of $TaSe_3$ turn out to be (1;100).

In view of the fact that the hallmark of topological non-trivial property is the existence of topological nontrivial surface states, the tight-binding Hamiltonians of semi-infinite samples are constructed by the maximally localized Wannier functions (MLWFs) for all the Ta d and Se p orbitals, which are generated from the first-principles calculations. The surface Green's functions of the semi-infinite sample are obtained using an iterative method[41]. The local DOS (LDOS), extracted from the imaginary part of the surface Green's function, is used to analyze the surface band structures. For STIs, the existence of an odd number of Dirac cones on the surface is ensured by the strong topological index $\nu_0 = 1$. On the (010) surface of $TaSe_3$, a Dirac cone is obtained at $\bar{B}$ point in Fig. 4(a), which hosts helical spin texture at the energy contour ($E = E_F$) in Fig. 4(c). On the $(10\bar{1})$ surface, a Dirac cone is found at $\tilde{X}$ point, as shown in

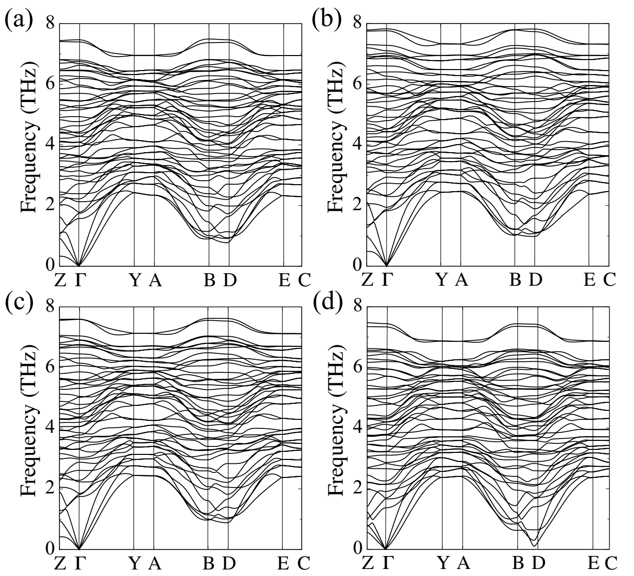

FIG. 6. (Color online) Phonon dispersion of $TaSe_3$ with c=1.0 c_0, c=0.95c_0 (P1), c=0.97c_0 (P2) and c=1.05c_0 (P3), as shown in (a), (b), (c) and (d), respectively.

Fig. 4(b) and its zoom-in plot in Fig. 4(d). The existence of a single Dirac cone on the surfaces is consistent with the STI phase.

Since it's a layered structure with trigonal-prismatic chains going in the *b*-direction, the lattice parameters in *a*- and *c*-directions are supposed to be more sensitive to temperature or strain than that in the *b*-direction. Therefore, the strain effects along the *a*- and *c*-directions have been systematically investigated in our calculations, in order to check the stability of the STI phase. For each given lattice constant, the internal positions of the atoms are fully relaxed until the force on each atom satisfies the required precision. The computed phase diagram is shown in Fig. 5(a) as a function of lattice parameters *a* (horizontal axis) and *c* (vertical axis). On the vertical dashed line in Fig. 5(a) (*i.e.*, the strain in the *a*-direction is zero), when *c* grows from 0.95c_0 to 1.05c_0 (with c_0 the lattice parameter without strain), it changes from a normal insulating (NI) phase, to STI phase, and then to WTI phase due to band inversion happening at TRIMs successively. Explicitly, at the beginning ($c = 0.95c_0$), no band inversion is found in Fig. 5(b) and the system is a trivial insulator. When $c = 0.97c_0$, two bands of opposite parity become touching at B point, as shown in Fig. 5(c), resulting in a Dirac semimetal phase at the phase transition point. After the transition point, the system enters STI phase. By increasing *c* further (*e.g.* $c = 1.05c_0$), another band inversion occurs at Z point, the system turns to WTI phase, as shown in Fig. 5(d). As we can see in Fig. 5(a), both STI (green) and WTI (red) phases survive in a considerable region compared with the NI (blue) phase. The phase boundaries are Dirac semimetals, which may also be observed in experiments. The phase diagram provides us an important roadmap to regulate the topological phase transitions in $TaSe_3$. Compared with the reported topological materials, $TaSe_3$ has two unique features. First, the compressive strain can remove the band inversion, which is different from the common concept that the compressive strain usually enhances the band inversion[42–44]. The compressive strain shortens the distances of the bonds of Ta1-Se3 and Ta2-Se6, the hybridization becomes stronger and the average gap ΔE is enlarged between Se_A p_z (Se_B p_z) and Ta_A d_{z^2} (Ta_B d_{z^2}) states. Second, many TIs have an *sp*-type band inversion or a *pp*-type band inversion[42–44], while $TaSe_3$ has a *pd*-type band inversion. Third, most TIs only have band inversion at one TRIM point (such as the Γ point)[28,45], while $TaSe_3$ has band inversion at three TRIM points, which leads to fruitful nontrivial phases under different strains, including 3D STI, 3D WTI and Dirac semimetal.

Next, we would like to discuss the possible CDW in $TaSe_3$. It is well-known that no CDW is observed in NbS_2. However, the phonon dispersion shows imaginary frequencies based on first-principles calculations[46]. In order to exclude the possibility of the "latent" CDW instability and greatly support our predictions of nontrivial topological properties in $TaSe_3$, we carefully calculate the phonon dispersion for $TaSe_3$, which is shown in Fig. 6(a). No imaginary frequency is found in the dispersion. The phonon calculations have also been checked with respect to many parameters, such as *k*-point grid, type of smearing and size of supercell etc. In addition, we also calculate the phonon dispersion of $TaSe_3$ with c=0.95c_0 (P1), c=0.97c_0 (P2) and c=1.05c_0 (P3), as shown in Fig. 6(b), 6(c) and 6(d), respectively. No imaginary frequency can be found in any of them. Therefore, it is safe to exclude the effect of CDW in $TaSe_3$.

IV. DISCUSSION AND CONCLUSION

To achieve topological superconductivity, it is challenging to find a material with both nontrivial topology of the electronic structure and superconductivity. A prior theoretical proposal of intrinsic non-trivial material is high-T_c superconductor $FeTe_xSe_{1-x}$[16] with $x = 0.5$ supporting topological surface states at E_F. Very recently, the topological superconducting phase has been verified on (001) surface by spin-resolved ARPES experiments[20]. Here we show another promising candidate $TaSe_3$, whose superconductivity has been reported for many years[7–9], is topologically non-trivial and has spin-momentum locking states on the surface. Compared to the $FeTe_xSe_{1-x}$ system, $TaSe_3$ does not require doping to introduce superconductivity, implying this superconductor can be grown in high-quality single crystals. At the Fermi level (μ_1), as we show in Fig. 4(c), the surface states are well separated from the bulk states. Based on Fu-Kane's proposal, the superconducting states of the surface states induced by the bulk superconductivity below T_c=2.3 K can be topologically nontrivial. However, if the chemical potential lies 40 meV (μ_2) below the Fermi level in Fig. 4(a), the surface states merge into the bulk states, which could kill the topological superconducting state and make the surface topological superconducting state sensitive to the position of the chemical potential. The future experimental work is needed to search for the potential topological superconductivity in the system.

In conclusion, we have calculated the electronic structure, and topological properties of TaSe$_3$ with $P2_1/m$ crystal structure by using density functional theory. The calculated topological invariants are (1;100), which indicate that it belongs to the STI phase. A single Dirac cone is obtained in the calculated surface spectra. Further systematical calculations of strain effects suggest TaSe$_3$ can realize multiple topological non-trivial phases under strains, including STI, WTI and Dirac semimetal phases. These topological non-trivial phases survive in a wide range of the strain along the a- and c-axes, making TaSe$_3$ an attractive platform to study the topological phase transitions. In addition, the co-existence of the topological phases and superconductivity of TaSe$_3$ suggests that it could be a realistic system to study the interplay between topological and superconducting phases in the future.

ACKNOWLEDGMENTS

We thank Prof. Robert J. Cava for useful discussions. F. B. P. and S. N. were supported by Stanford Energy 3.0. W. X. was supported by LSU-startup funding and the Louisiana Board of Regents Research Competitiveness Subprogram (RCS) under Contract Number LEQSF (2017-20)-RD-A-08. Z. W. was supported by the Department of Energy Grant No. DE-SC0016239, the National Science Foundation EAGER Grant No. NOA-AWD1004957, Simons Investigator Grants No. ONR-N00014-14-1-0330, No. ARO MURI W911NF-12-1-0461, and No. NSF-MRSEC DMR- 1420541, the Packard Foundation, the Schmidt Fund for Innovative Research, and the National Natural Science Foundation of China (No. 11504117). L.X. and R.J. are supported by Department of Energy Grant No. SC00i6315.

---

[*] zjwang@princeton.edu

[1] K. Tsutsumi, T. Takagaki, M. Yamamoto, Y. Shiozaki, M. Ido, T. Sambongi, K. Yamaya, and Y. Abe, Physical Review Letters **39**, 1675 (1977).

[2] J. Wilson, Physical Review B **19**, 6456 (1979).

[3] R. J. Cava, R. Fleming, R. Dunn, and E. Rietman, Physical Review B **31**, 8325 (1985).

[4] S. Srivastava and B. Avasthi, Journal of materials science **27**, 3693 (1992).

[5] T. Ekino and J. Akimitsu, Japanese Journal of Applied Physics **26**, 625 (1987).

[6] P. Haen, F. Lapierre, P. Monceau, M. N. Regueiro, and J. Richard, Solid State Communications **26**, 725 (1978).

[7] T. Sambongi, M. Yamamoto, K. Tsutsumi, Y. Shiozaki, K. Yamaya, and Y. Abe, Journal of the Physical Society of Japan **42**, 1421 (1977).

[8] M. Yamamoto, Journal of the Physical Society of Japan **45**, 431 (1978).

[9] S. Nagata, H. Kutsuzawa, S. Ebisu, H. Yamamura, and S. Taniguchi, Journal of Physics and Chemistry of Solids **50**, 703 (1989).

[10] E. Canadell, I. Rachidi, J. Pouget, P. Gressier, A. Meerschaut, J. Rouxel, D. Jung, M. Evain, and M. Whangbo, Inorganic Chemistry **29**, 1401 (1990).

[11] F. Wilczek, Nature Physics **5**, 614 (2009).

[12] M. Leijnse and K. Flensberg, Semiconductor Science and Technology **27**, 124003 (2012).

[13] A. Y. Kitaev, Annals of Physics **303**, 2 (2003).

[14] L. Fu and C. L. Kane, Physical review letters **100**, 096407 (2008).

[15] B. Yan, M. Jansen, and C. Felser, Nature Physics **9**, 709 (2013).

[16] Z. Wang, P. Zhang, G. Xu, L. Zeng, H. Miao, X. Xu, T. Qian, H. Weng, P. Richard, A. Fedorov, *et al.*, Physical Review B **92**, 115119 (2015).

[17] X. Wu, S. Qin, Y. Liang, C. Le, H. Fan, and J. Hu, Physical Review B **91**, 081111 (2015).

[18] L. M. Schoop, L. S. Xie, R. Chen, Q. D. Gibson, S. H. Lapidus, I. Kimchi, M. Hirschberger, N. Haldolaarachchige, M. N. Ali, C. A. Belvin, *et al.*, Physical Review B **91**, 214517 (2015).

[19] G. Xu, B. Lian, P. Tang, X.-L. Qi, and S.-C. Zhang, Physical Review Letters **117**, 047001 (2016).

[20] P. Zhang, K. Yaji, T. Hashimoto, Y. Ota, T. Kondo, K. Okazaki, Z. Wang, J. Wen, G. Gu, H. Ding, *et al.*, arXiv preprint arXiv:1706.05163 (2017).

[21] Q. Xu, Z. Song, S. Nie, H. Weng, Z. Fang, and X. Dai, Physical Review B **92**, 205310 (2015).

[22] Y. Xing, H. Wang, C.-K. Li, X. Zhang, J. Liu, Y. Zhang, J. Luo, Z. Wang, Y. Wang, L. Ling, *et al.*, npj Quantum Materials **1**, 16005 (2016).

[23] Y.-Q. Wang, X. Wu, Y.-L. Wang, Y. Shao, T. Lei, J.-O. Wang, S.-Y. Zhu, H. Guo, L.-X. Zhao, G.-F. Chen, *et al.*, Advanced Materials **28**, 5013 (2016).

[24] A. Das, Y. Ronen, Y. Most, Y. Oreg, M. Heiblum, and H. Shtrikman, Nature Physics **8**, 887 (2012).

[25] Y. S. Hor, A. J. Williams, J. G. Checkelsky, P. Roushan, J. Seo, Q. Xu, H. W. Zandbergen, A. Yazdani, N. Ong, and R. J. Cava, Physical review letters **104**, 057001 (2010).

[26] L. A. Wray, S.-Y. Xu, Y. Xia, Y. San Hor, D. Qian, A. V. Fedorov, H. Lin, A. Bansil, R. J. Cava, and M. Z. Hasan, Nature Physics **6**, 855 (2010).

[27] H. Zhang, C.-X. Liu, X.-L. Qi, X. Dai, Z. Fang, and S.-C. Zhang, Nature physics **5**, 438 (2009).

[28] W. Zhang, R. Yu, H.-J. Zhang, X. Dai, and Z. Fang, New Journal of Physics **12**, 065013 (2010).

[29] M. Z. Hasan and C. L. Kane, Reviews of Modern Physics **82**, 3045 (2010).

[30] X.-L. Qi and S.-C. Zhang, Reviews of Modern Physics **83**, 1057 (2011).

[31] L. Fu, C. L. Kane, and E. J. Mele, Physical Review Letters **98**, 106803 (2007).

[32] P. Blaha, K. Schwarz, G. Madsen, D. Kvasnicka, and J. Luitz, WIEN2k, An Augmented Plane Wave Plus Local Orbitals Program for Calculating Crystal Properties (TU Vienna, Vienna, 2001).

[33] F. Tran and P. Blaha, Physical Review Letters **102**, 226401 (2009).

[34] G. Kresse and J. Furthmüller, Computational Materials Science **6**, 15 (1996).

[35] G. Kresse and J. Furthmüller, Physical Review B **54**, 11169 (1996).

[36] A. Togo, F. Oba, and I. Tanaka, Physical Review B **78**, 134106 (2008).

[37] R. Nesper, Zeitschrift für anorganische und allgemeine Chemie **640**, 2639 (2014).

[38] J. O. Island, A. J. Molina-Mendoza, M. Barawi, R. Biele, E. Flores, J. M. Clamagirand, J. R. Ares, C. Sánchez, H. S. van der Zant, R. DAgosta, *et al.*, 2D Materials **4**, 022003 (2017).

[39] R. Buhrman, C. Bastuscheck, J. Scott, J. Kulick, D. Gubser, T. Francavilla, S. Wolf, and J. Leibowitz, in *AIP Conference Proceedings*, Vol. 58 (AIP, 1980) pp. 207–215.

[40] E. Bjerkelund, J. Fermor, and A. Kjekshus, Acta Chemica Scandinavica **20**, 1836 (1966).

[41] N. Marzari, A. A. Mostofi, J. R. Yates, I. Souza, and D. Vanderbilt, Reviews of Modern Physics **84**, 1419 (2012).

[42] Y. Nie, M. Rahman, D. Wang, C. Wang, and G. Guo, Scientific Reports **5**, 17980 (2015).

[43] E. T. Sisakht, F. Fazileh, M. Zare, M. Zarenia, and F. Peeters, Physical Review B **94**, 085417 (2016).

[44] D. Shao, J. Ruan, J. Wu, T. Chen, Z. Guo, H. Zhang, J. Sun, L. Sheng, and D. Xing, Physical Review B **96**, 075112 (2017).

[45] S.-M. Nie, Z. Song, H. Weng, and Z. Fang, Physical Review B **91**, 235434 (2015).

[46] C. Heil, S. Poncé, H. Lambert, M. Schlipf, E. R. Margine, and F. Giustino, Physical review letters **119**, 087003 (2017).